Ceramic Topcoats of Plasma-Sprayed Thermal Barrier Coatings: Materials, Processes, and Properties

Emine Bakan, Robert Vaßen*

Forschungszentrum Jülich GmbH, Institute of Energy and Climate Research IEK-1, 52425 Jülich, Germany

*Corresponding Author. Forschungszentrum Jülich GmbH, Institute of Energy and Climate Research IEK-1, 52425 Jülich, Germany. Tel: +49 2461 61 6108, Fax: +49 2461 61 2455, e-mail: r.vassen@juelich.de.

Abstract

The ceramic topcoat has a major influence on the performance of the thermal barrier coating systems (TBCs). Yttria-partially-stabilized zirconia (YSZ) is the topcoat material frequently used and the major deposition processes of the YSZ topcoat are atmospheric plasma spraying (APS) and electron beam physical vapor deposition (EB-PVD). Recently, also new thermal spray processes such as Suspension Plasma Spraying (SPS) or Plasma Spray – Physical Vapor Deposition (PS-PVD) have been intensively investigated for TBC topcoat deposition. The first section of the article will review these new processes and will describe especially the different microstructures that can be obtained. Furthermore, the properties and the intrinsic–extrinsic degradation mechanisms of the YSZ will be discussed.

In the second section, alternative ceramic materials to the YSZ such as perovskites and hexaaluminates, which were investigated mainly due to the limited high-temperature capability of the YSZ, will be summarized, while properties of pyrochlores with regard to their crystal structure will be discussed more in detail. The merits of the pyrochlores such as good CMAS resistance and their weaknesses, e.g. thermochemical incompatibility with alumina thermally grown oxide, as well as processability issues will be outlined.

1. Thermal Barrier Coatings

Thermal barrier coatings (TBCs) are protective coatings applied to the surface of hot metallic sections in gas-turbine engines. The major fields of the application of gas turbines in which the TBCs are utilized are aircraft propulsion and power generation. In 2016, the market forecasters estimated an impressive production of nearly 228,000 aviation gas turbine engines valued in $1.232 trillion through 2030 and of 5,480 power generation gas turbine engines worth $105.3 billion over the next 10 years [1,2]. A recent BBC report [] showed a market volume for TBC coatings of 835 Mill $ in 2016, thereof 334 Mill $ EB-PVD, 168 Mill $ APS and the rest other thermal spray technologies. The volume is expected to increase with an annual growth rate of 5.6% over the next 5 years. Considering these figures, it is only rational to estimate a rising demand for the protective coating technologies in the near future.

The conventional TBCs systems consist of a ceramic topcoat (i), a metallic bond coat (ii), and a thermally grown oxide “TGO" layer (iii) that forms due to oxidation of the bond coat as a result of oxygen inward diffusion through the top coat at TBC operation temperatures. The aluminum-rich bond coat ((Ni, Co)CrAlY or aluminides of Pt and Ni), which forms the alumina (α-Al_2O_3) TGO layer on top, has the primary function of protecting the substrate from oxidation. Providing the thermal insulation in the TBC system is the main function of the ceramic topcoat layer. Since it was introduced in the 1970s [3], 6-8 wt. % yttria-stabilized zirconia (7YSZ) has been the material of choice for ceramic top coats, as it has the exceptional combination of desired properties (section 2.1). Was YSZ used in 1970, not MgO/ZrO2

TBC are complex systems bringing the metallic and ceramic materials together, to function under highly demanding thermal cycling conditions. To that end, ceramic materials are further enhanced both in terms of thermal insulation efficiency and thermal expansion compliance in different ways and extend by different processing routes. Atmospheric plasma spray (APS) and electron beam-physical vapor deposition (EB-PVD) are two established methods, while newer thermal spray techniques such as suspension plasma spray (SPS) and plasma spray-physical vapor deposition (PS-PVD) are under development showing attractive properties (section 2.2).

Even though the 7YSZ remained as the state of the art for decades, its temperature limitation at about 1200°C (section 2.3) has been the main motivation to modify it chemically or to substitute it with new ceramic materials to further boost engine efficiency. Therefore, new ceramic compositions were extensively studied, yet in many of these materials with high-temperature stability, other critical issues such as interdiffusion with alumina TGO were observed. This introduced the double ceramic layer concept to the TBC literature, combining the benefits of YSZ and new materials. Furthermore, deposition of several of these complex oxides with stoichiometric compositions was found to be not so easy both with thermal spray and vapor phase deposition processes, implying a demand for more careful process optimizations (section 3.1-4).

2. YSZ Ceramic Topcoat

2.1. Properties

A *good thermal stability*, a *low thermal conductivity*, a *high coefficient of thermal expansion* (CTE) in combination with a *high fracture toughness* are the main required properties for the ceramic top coat on top of metallic components. The YSZ has a high melting point (2700 °C) and one of the lowest thermal conductivities of all ceramics at elevated temperatures; the conductivity of bulk YSZ and YSZ coatings with different microstructures and porosity were reported to be 2.6 W/mK (5.3 wt. % YSZ, 600 °C) [4] and 0.7-1.4 W/mK (7.25 wt. % YSZ) [5], respectively. The YSZ also has a high CTE (11 x 10^{-6} K^{-1}), which is close to that of the underlying superalloy substrate (14 x 10^{-6} K^{-1}) [6] and helps to mitigate stresses arising from the thermal-expansion mismatch. But a mismatch still remains and these stresses lead to crack propagation within the coatings regardless of the high toughness as observed in 4-5 YSZ due to its ferroelastic switching [7]. Therefore, mainly by trying to reduce the stress levels and/or increasing the strain tolerance of the coatings, a further improvement of the coating performance is desired. This can be achieved by introducing porosity and cracks (inter-lamellar cracks, segmentation cracks etc.) into the coatings or depositing columnar structures as will be discussed below.

2.2. Deposition Technologies and Microstructure

Atmospheric plasma spraying (APS) and electron beam – physical vapor deposition (EB–PVD), two standard processing techniques for the top coat deposition, both enhance the thermal insulation efficiency and thermal expansion compliance of the ceramic materials in different ways and extents. As in this article the focus are thermal spray technologies the EB-PVD process is not further discussed, further information can be found e.g. in [].

2.2.1 Athmospheric plasma spraying process

In the APS process, an electric arc generated between anode and cathode ionizes the flowing process gasses (argon, hydrogen, nitrogen or helium) into the plasma state (**Figure 1, left**). The ceramic powder particles are injected into this plasma jet where they are heated and accelerated towards the substrate so that the molten or partly molten particles impact the surface of the substrate at high speed. This leads to deformation of the particles and spread like pancakes or so-called splats (1 to 5 µm thick, 200 to 400 µm diameter) [8,9]. Heat from the hot particles is transferred to the cooler substrate material and the splats rapidly solidify and shrink. Due to hindered contraction of the splats on the substrate or on the previously deposited layer, tensile quenching stresses arise within the splats and mainly relaxed by micro-cracking [10]. As a result of quenching stresses as well as imperfect splat contacts, a coating microstructure with typical inter-splat, intra-splat cracks, and larger spherical pores is deposited on the substrate in the plasma spray process (**Figure 1, right**). Such microstructure with 10-20 volume % cumulative porosity lowers the thermal conductivity (in particular the inter-splat cracks aligned parallel to the substrate surface and normal to the heat flux, typical 0.7 to 1.0 W/m/K) and the elastic modulus of the ceramic top coat for a better thermal insulation and thermo-mechanical performance, respectively. Additionally, the micro cracks allow partial sliding of the individual splats along their boundaries and a kind of stress release even at room temperature takes place by that process [11]. Therefore, spray parameters such as spray torch power, plasma gas composition, and spray distance, which affect melting states and velocities of the particles, or temperature of the substrate determining the cooling rates of the splats on arrival are carefully tuned to achieve the desired porous microstructures. It should be also mentioned here that, other than the specific spraying

conditions leading to high porosity levels, today it is well known to use plastic-ceramic powder mixtures for the same purpose [12,13].

Figure 2 illustrates the stress development in a porous, micro-cracked coating, which is deposited on a superalloy substrate, during a thermal cycle. When this system is heated, tensile stresses develop in the coating (1) due to the larger thermal expansion coefficient of the substrate. At high temperature, stress relaxation and sintering of the coating takes place, the former leading to a reduction of the thermal stress (2), the latter leading to a steeper slope during cooling (3). Both factors increase the compressive stress level at room temperature which might be slightly reduced by room temperature relaxation (4).

This stress development in the coatings becomes more critical if the thickness of the coating (d_{coat}) is desired to be as high as in the millimeter range. Because driving force for the crack propagation is the elastic energy stored in the coating and can be described by the energy release rate (G) [14].

$$G = \frac{(1-n^2)\,\sigma_{coat}^2\,d_{coat}}{2\,(1-n)^2\;E_{coat}} = \frac{(1-n^2)}{2\,(1-n)^2}\,\Delta\varepsilon^2 E_{coat} d_{coat} \qquad (1)$$

For a given strain ($\Delta\varepsilon$), which is determined by the thermal expansion mismatch between coating and substrate and the relaxation at high temperatures, the energy release rate is proportional to the d_{coat} and inversely proportional to elastic modulus of the coating (E_{coat}) and an additional factor which is a function of the Poisson´s ratio (ν). For that reason, a further increase in the porosity levels (>20%) of high-thickness coatings is required to lower the E_{coat}, and as a result to obtain sufficiently low driving force for crack propagation.

2.2.2 Segmented coating by atmospheric plasma spraying

Another efficient way to reduce the energy release rate especially for thick coatings is the introduction of segmentation cracks, which are the vertical cracks running perpendicular to the coating surface. These systems are also called as dense vertically cracked (DVC) TBCs and they were developed more than 20 years ago [15]. Vertical cracks can be formed in the top coat by specific, hot spray conditions which allow

a good bonding between the splats and only limited micro-crack formation. As a result, large tensile stresses are developed in these dense coatings which relax by the formation of segmentation cracks with typical densities in the order of 3-10 cracks/mm [16,17]. As shown in **Figure 2**, the presence of these cracks significantly reduces the mean stress level in the coating by opening during heating period, and hence the relaxation at high temperature also becomes limited. Moreover, the already rather dense structure only shows limited further increase of the elastic modulus. However, due to dense structure, the thermal conductivity of these coatings are relatively high (typically 1.3–1.8 W/m/K) compared to their micro-cracked counterparts. Similarly, the columnar structure of EB-PVD coatings, which is obtained by the condensation of vaporized coating material on the surface of a heated substrate, exhibits a great strain tolerance (**Figure 2**) but also a higher thermal conductivity due to the presence of columnar gaps [18]. Therefore, generally, EB-PVD coatings are preferred because of their greater strain tolerance for the applications where frequent thermal cycling will occur, even though they are inferior to APS coatings regarding thermal insulation.

2.2.3 Segmented and columnar coatings by suspension plasma spraying

Another thermal spray technology which can generate segmented coatings with a rather high porosity level is the Suspension Plasma Spray (SPS) process [19]. Here a suspension of submicron ceramic particles instead of the powderous micron-sized feedstock is used. Also, precursors as metal salts have been employed (so-called solution precursor plasma spraying (SPPS) [20]. The finer size of the deposited droplets allow the generation of different microstructures, especially a high segmentation crack density (even above 10 cracks/mm [21]) and a high cumulative porosity mainly consisting of sub-micrometer range pores [22]) (**Figure 3, left**). As a result of this microstructure, the thermal conductivity of SPS coatings is in a similar range with that of APS porous coatings and lower than the one of APS segmented coatings. The thermal shock resistance and thermal cyclic performance of the SPS coatings can be excellent [23,24]. Recently, it also was discovered that the SPS process allows the formation of columnar structures. Under certain process conditions, the fine droplets will follow the process gas flow parallel to the surface of the substrate and will impinge on obstacles leading to the formation of columns [25] (**Figure 3, right**). Also

these coatings can show excellent thermal cycling performance [] and additionally a non-line of sight capacity which is favourable for the coating of complex shaped components.

In the last years the SPs process has also successfully been used to deposit different thermal barrier coating materials as perovskites [] and pyrochlores [] as segmented or columnar structured coatings.

2.2.4 Columnar coatings by plasma spray physical vapour deposition

A rather new thermal spray technology is the plasma spray-physical vapor deposition (PS-PVD). It uses a high-energy plasma gun operated in an inert atmosphere at reduced work pressures (50-200 Pa) which enables the vaporization of fine feedstock material and can produce columnar like structures by a vapor phase deposition similar to the EB-PVD process (**Figure 4**). In addition to the high strain tolerance microstructure, the PS-PVD offers lower investment costs and higher deposition rates than the EB-PVD along with the ability of coating complex geometries and shadowed areas [26]. This is possible due to the gas flow giving a non-line-of-sight characteristic. It was demonstrated that thermal cycling lifetimes more than two times higher than conventionally sprayed TBCs were obtained with optimized PS-PVD process conditions [27]. With the use of suitable feedstock materials also other TBC materials can be processed by PS-PVD. An example using Gd2Zr2O7 is given in [] showing the excellent performance of the coating as a double layer YSZ/GZO system (see section 3.4.6).

2.3. Degradation

The newer thermal spray technologies seem already to surpass the capabilities of the APS presenting highly strain tolerant and porous coatings. On the other hand, maintenance of strain tolerance and porosity requires the *sintering resistance* and *phase stability* of the top coat material at high application temperatures. Unfortunately, the YSZ shows insufficient phase stability and accelerated sintering at temperatures above 1200 °C, which are the dominant degradation mechanisms of the plasma sprayed ceramic YSZ top coat [8,28,29]. At room temperature, a non-equilibrium, high-yttria containing tetragonal phase (t', also called non-transformable tetragonal) is observed in as-sprayed YSZ coatings. The t' phase is formed due to rapid cooling during the deposition process, which kinetically suppresses the formation of equilibrium phases (low-yttria containing transformable tetragonal and high-yttria containing cubic), and therefore very small

amounts of the equilibrium phases are observed in the as-sprayed microstructures. However, the t' phase undergoes phase separations into the equilibrium phases at high temperatures resulting in degradation of the coating [30]. Because the transformation of the low-yttria-containing tetragonal phase into the monoclinic phase upon cooling is accompanied by a volume change [31,32] and the high-yttria-containing cubic phase has low toughness [33,34]. Furthermore, the enhanced sintering and resultant densification above 1200°C lowers the thermal resistance and increases the elastic modulus [35].

Similar to the thermomechanical compatibility of the components in the TBC system, *thermochemical compatibility* is also a critical factor for the durability. Interactions between the TGO and ceramic top coat can result in replacing the alumina with less protective oxides and hence can be deleterious for the system. However, the solubility of YSZ (up to 20 wt.% yttria addition) and alumina in each other is reported to be very limited up to 1250°C [36,37].

In addition to intrinsic issues leading to degradation of the TBC system, there are also extrinsic degradation mechanisms such as *erosion*, *FOD (foreign object damage)*, *hot corrosion* and *CMAS* (initials of calcium-magnesium alumina-silicate) attack. Erosion and FOD are leading to the progressive loss of thickness and total coating removal, respectively [38]. Small particles ingested into turbines and internally generated larger particles (such as engine wear residues, thermally spalled TBC from the combustor) contribute to erosion damage, while any foreign objects such as rocks, ice from the wings in case of FODcan they go through the compressor? impact the components of the engine and can have disastrous consequences. Hot corrosion of TBC occurs due to molten deposits resulting from impurities in the fuel; the impurities such as sodium, sulfur, vanadium, lead and phosphorus are oxidized during combustion to form strong acidic or alkaline oxides that attack both the ceramic and metallic components of the TBC system. It was found that the Y_2O_3 in YSZ thermal barrier coatings react strongly with the V_2O_3 resulting in formation of YVO_4, which depletes yttria from the zirconia matrix and causes the spallation of TBC [39]. Furthermore, molten oxides permeate to the bond coat through the YSZ top coat and lead to accelerated oxidation of the bond coat [?]. Different approaches were introduced to improve the corrosion resistance of YSZ such as altering the yttria content or the stabilizer of the zirconia matrix. Scandia- yttria-stabilized zirconia was found to be

more corrosion resistant to vanadate hot corrosion, but also some stabilization issues of it was reported by Jones et al.[40].

A similar degradation mechanism at high operation temperatures is caused by the environmentally ingested airborne sand/ash particles melt on the hot TBC surfaces resulting in the deposition of the CMAS glass deposits [41-43]. At high surface temperatures, the CMAS rapidly penetrate the porosity of the coating and lead to premature failure of the coating as a consequence of mechanical and chemical interactions. Former leads to loss of strain tolerance and stiffening of the YSZ coating, while the latter result in the destabilization of the YSZ. Due to the presence of the CMAS in the structure with much lower CTE than the YSZ top coat and metallic components, large compressive stresses develop upon cooling increasing further the energy release rate of the system. CMAS was also reported to lower the yttria content of the YSZ, which results in the formation of transformable monoclinic zirconia as discussed above and consequently compromising the integrity of the system [43]. From a mechanical point of view, the CMAS induced degradation relies on progressing of the molten deposits through the pores of the top coat surface. Therefore the surface porosity of the top coat becomes critical and makes EB-PVD top coat microstructures particularly vulnerable to the CMAS attack. From a chemical perspective, Aygun et al. [44] showed that up to 20 mol.% Al_2O_3 and 5 mol.% TiO_2 additions into YSZ enable to mitigate CMAS attack by incorporation of both Al and Ti solutes within CMAS glass. Later, it was also shown that increasing the yttria content of zirconia increase the CMAS resistance [45] although other issues related to phase stability are manifested in that case. Recently, more general concepts have been developed to get a clearer insight into the complex degradation mechanisms by CMAS. A more detailed discussion will follow in section 3.4.5.

3. Alternative Ceramic Topcoat Materials

Over the last 15 years, primarily four different ceramic material groups; (i) zirconia doped with different rare-earth (RE) cations (defect cluster TBC's), (ii) perovskites, (iii) hexaaluminates, and (iv) pyrochlores have been suggested as promising new top coat materials (see **Table 1** for the chemical compositions). Some other materials e.g. mullite [46], silicates ($ZrSiO_4$ [6]), garnets ($Y_3Al_5O_{12}$ YAG [47], $Y_4Al_2O_9$ YAM

[48]), $(Ca_{1-x}Mg_x)Zr_4(PO_4)_6$ [49], were also considered as candidate materials however their typically low CTE preclude the possibility of their application.

3.1. Defect cluster TBCs

In defect-cluster TBC's, the zirconia is doped with oxides of the different RE-cations. Due to a significant difference between the ionic sizes of the zirconia and RE, a highly defective lattice is produced while thermodynamic stability can be preserved. The obtained lattice distortion scatters lattice and radiative photon waves and hence reduces the thermal conductivity of the material. Zhu et al. [50] reported that the thermal conductivity of the standard ZrO_2-4.5 mol% Y_2O_3 could be reduced about 40% (from ~2.5 to 1.7 W/mK) when the zirconia doped with 5.5 mol% Y_2O_3-2.25 mol% Gd_2O_3-2.25 mol% Yb_2O_3. Furthermore, good thermal cycling performances of the defect cluster zirconia with low dopant concentrations were observed. However, decreasing cyclic lifetimes were monitored when the dopant concentrations were increased due to reduced fraction of tetragonal phase and hence reduced toughness values [51].

3.2. Perovskites

The perovskites were considered as candidate materials mainly due to their refractory properties (melting point, $SrZrO_3$; 2650 °C, $Ba(Mg_{1/3}Ta_{2/3})O_3$; 3100 °C). Their CTE higher than 8.5 x 10^{-6} K^{-1} and thermal conductivity lower than 2.2 W/mK were also found to be advantageous for TBCs. However, later it was observed that complex perovskites (e.g. $Ba(Mg_{1/3}Ta_{2/3})O_3$, $La(Al_{1/4}Mg_{1/2}Ta_{1/4})O_3$) decomposes during spraying and hence the deposit is often accompanied by secondary phases, while $SrZrO_3$ undergoes some phase transformations and the one from orthorhombic to pseudo-tetragonal which occurs at 740 °C involves a volume change of ~0.14 % [52-54]. Ma et al. reported that doping the $SrZrO_3$ with Yb_2O_3 and Gd_2O_3 not only suppresses the phase transformation but also lowers the thermal conductivity of $SrZrO_3$ (~20 %). This modification also yields longer cyclic lifetimes than the standard YSZ particularly in a *double layer* structure above 1300°C [55].

The double-layer structure describes a two-layer ceramic coating system (YSZ and an alternative material on top of it with high-temperature stability such as perovskite, pyrochlore etc.). The YSZ layer between the

TGO and the alternative ceramic material was introduced to solve thermochemical incompatibility problems with the TGO but more often to take advantage of high toughness of the YSZ close to the TGO (**Figure 5**). Because crack propagation in the alternative materials is known to be easier than the YSZ. Therefore, today it is a well-accepted approach and successful examples combining different materials with the YSZ and using different deposition methods (APS, EB-PVD) can be found in the literature [55-59].

3.3. Hexaaluminates

Among the hexaaluminates, lanthanum hexaaluminate (LHA) with defective magnetoplumbite structure, which crystallizes in the form of plate-like grains, is the most investigated material for TBCs. Because in addition to a similar thermal conductivity to the YSZ (2.6 W/mK), it offers a low Young's modulus, significantly high sintering resistance, structural and thermochemical stability up to 1400 °C [60,61]. Furthermore, due to partial amorphicity of the coatings made of different hexaaluminate compositions (particularly pronounced for $LaLiAl_{11}O_{18.5}$) in the as-sprayed state, formation of a segmentation crack network in the coatings was observed after heat treatments [62]. As a result of this good combination of properties, good lifetime performances were reported for this material [63]. More recently, another hexaaluminate $LaTi_2Al_9O_{19}$ was conceived as a novel TBC material [64] due to its low thermal conductivity (1.0-1.3 W/mK) and phase stability up to 1600°C. The CTE of the $LaTi_2Al_9O_{19}$ was reported in the range of 8-12x10^{-6} K^{-1} (200-1400°C), which is also comparable to that of the YSZ. Nevertheless, no significant improvement in the performance was monitored when the $LaTi_2Al_9O_{19}$ is implemented as a single layer (<200 cycles at 1300°C) due to its low fracture toughness. However, the performance was significantly advanced in a double layer system (1375 cycles at 1300°C).

3.4. Pyrochlores

According to Web of Science™, among the four aforementioned group, the most extensively investigated group for TBCs is the pyrochlores. **Figure 6** demonstrates the significant increase in the number of the publications covering the pyrochlores within the years in comparison with its counterparts. The increasing popularity of the pyrochlores can be justified with their good combination of properties such as low thermal

conductivity and high-temperature phase stability but mostly with their pronounced CMAS resistance. These properties of pyrochlores with regard to their crystal structure as well as some implementation issues will be discussed more in detail below.

3.4.1. Crystal Structure

The pyrochlore crystal structure ($A_2B_2O_7$ or $A_2B_2O_6O'$, A and B are 3+ or 2+ and 4+ or 5+ cations) with $Fd\bar{3}m$ space group is typically described by using its similarity to simple fluorite structure (**Figure 7**). In the ideal fluorite structure (MO_2, $Fm\bar{3}m$), the oxygen ions are located in the equivalent tetrahedral sites of an M face-centered cubic array. Similarly, in pyrochlores, two types of A and B cations form the face-centered cubic array exhibiting an alternating ABAB order at 16c and 16d sites in <110> directions, which result in doubling of the lattice parameter (a) with respect to the fluorite structure. However due to this cation ordering in the pyrochlores, tetrahedral anion sites are no longer crystallographically identical; three distinct tetrahedral sites exist in the structure: the 48f, the 8a, and the 8b. Six oxygen atoms occupy the 48f sites with two A and two B neighbors, while the seventh oxygen occupies the 8b site surrounded by four A cations. The 8a site remains vacant, thereby 87.5% of the tetrahedral sites are filled in the pyrochlore structure while in the ideal fluorite all of them are occupied [65].

The stability of the A3+, B4+ type pyrochlore structure (A is a lanthanide and B is a transition metal) is governed by the ratio of the ionic radii of A and B cations ($1.46 \leq rA/rB \leq 1.80$). Accordingly, for instance, lanthanide zirconates (Ln: Gd→La) with the ionic radius ratio ranging from 1.46 to 1.61 adopts to pyrochlore structure, while lanthanide zirconates (Ln: Lu→Tb) with the ionic radius ratio ranging from 1.35 to 1.44 crystallize in defect fluorite structure. The ordered pyrochlore structure can be transformed to defect fluorite structure by a random distribution of both cations and anions onto their individual sublattice and such transformation can be induced by temperature, pressure, composition changes or ion radiation [66]. Effect of temperature and composition on the stability and relevant properties of lanthanide zirconates ($Ln_2Zr_2O_7$) for TBCs will be further discussed below.

3.4.2. Thermal conductivity

As a result of high concentration of intrinsic oxygen vacancies, high level cation substitution (vs. YSZ) and large atomic mass difference between zirconia and large lanthanides, which increases the phonon scattering strength of the point defects [67], $Ln_2Zr_2O_7$ (Ln: La, Nd, Sm, Eu, Gd) are attractive low-thermal conductivity material candidates. Their thermal conductivities were reported between 1.2-2.2 W/mK in different studies (**Table 2**), although significant discrepancies are visible between the studies investigating the same material, which can be attributed to the different method of sintering and hence differences in the initial porosities of samples. Recently Fabrichnaya et al. investigated the effect of sintering method on the measured thermal conductivities and demonstrated that the $Ln_2Zr_2O_7$ (Ln: La, Nd, Sm) samples sintered using the SPS/FAST (spark plasma sintering/field assisted sintering technique) have substantially higher thermal diffusivities and conductivities than that of the samples sintered conventionally at 1600 °C [68]. A thermal conductivity of 2.2 W/mK for the SPS/FAST $La_2Zr_2O_7$ was reported in this study, which is quite similar to that of the YSZ.

Further reductions in the thermal conductivity of the $Ln_2Zr_2O_7$ pyrochlores were achieved by cation dopings. Lehmann et al. showed that doping $La_2Zr_2O_7$ with 30 % Nd (atomic mass, ma=144.23), Eu (ma=151.94) or Gd (ma=157.25) leads to a systematic reduction in the thermal conductivity with the increase of ma of the doping element [69]. Accordingly, a maximum reduction from 1.55 to 0.9 W/mK in the thermal conductivity was obtained with 30 % Gd dopant at 800 °C. Bansal and Zhu also studied the thermal conductivity of the same material and revealed that doping $La_2Zr_2O_7$ with both Gd (15 %) and Yb (15 %) leads to additional reductions with respect to the solely Gd (30 %) doped $La_2Zr_2O_7$ [70]. More recently, Guo et al. reported the thermal conductivities of Yb_2O_3 (Yb, ma=173.05) doped $Gd_2Zr_2O_7$ ceramics as in a range of 0.88-1.00 W/mK at 1400 °C, about 20 % lower than that of $Gd_2Zr_2O_7$ (1.2 W/mK) [71].

Although many experimental studies, especially on $Ln_2Zr_2O_7$ pyrochlores, are already available, measurements are typically limited to 800 °C. If they are not, then a pronounced contribution of radiative heat transfer at higher temperatures complicates the interpretation and understanding of point defects and phonon scattering at these high temperatures. In this regard, molecular dynamic (MD) simulations are

shown to be useful for adapting and further developing earlier phonon models to get a better understanding of thermal transport in TBC materials. Schelling et al. investigated the effect of the size of A, B cations (A = La, Pr, Nd, Sm, Eu, Gd, Y, Er or Lu; B = Ti, Mo, Sn, Zr or Pb) on the thermal conductivity of forty different pyrochlore composition at 1200 °C and found a greater dependence on the B than A ionic radius [72]. Furthermore, while results of different experimental studies indicate $Gd_2Zr_2O_7$ with the lowest thermal conductivity (1.2 W/mK) in $Ln_2Zr_2O_7$ group (Ln: La, Nd, Sm, Eu, Gd), the simulation results suggest no systematic dependence of thermal conductivity on the size of the A ion, and predict $Nd_2Zr_2O_7$ as the most thermally insulating pyrochlore in this group. In the same study, some of the lanthanide-stannate pyrochlores and lanthanide-plumbate pyrochlores are predicted to have a lower thermal conductivity than lanthanide zirconates. However, Qu et al. measured the thermal conductivities of $Ln_2Sn_2O_7$ (Ln: La-Lu, Y) between 2.0-2.5 W/mK at 1000°C [73] and $Ln_2Pb_2O_7$ structures were reported to be unstable above 300°C [65].

3.4.3. High-Temperature Phase Stability

Another essential benefit of $Ln_2Zr_2O_7$ is their high-temperature phase stability. Unlike the YSZ, they remain as single phases over the entire service temperature range of the TBCs. **Table 2** shows maximum stability temperatures of different $Ln_2Zr_2O_7$ (Ln: La, Nd, Sm, Eu, Gd) compositions as well as their melting temperatures. The former indicate the temperature at which pyrochlore (P) transforms to a so-called defect fluorite structure (F), as mentioned earlier. Accordingly, the $Gd_2Zr_2O_7$ has the lowest stability temperature in this group at about 1550°C, and transformation temperature rises with increasing Ln cation size (Gd→Nb). In the La_2O_3-ZrO_2 system, the pyrochlore phase becomes stable all the way up to the liquidus temperature (2283°C) and thus no longer exhibits a solid state (F↔P) transition.

It should be mentioned here that when different pyrochlore compositions ($Ln_2Zr_2O_7$, Ln: La, Sm, Gd) were deposited on the substrates by plasma spraying, the as-sprayed coatings were found to be showing defect fluorite structure at room temperature [74-76]. This order-disorder transition is typically attributed to the high cooling rate of the molten particles in plasma spraying process, which could kinetically constrain the ordering process. Similarly, in EB-PVD process, as-deposited coatings were reported to be in defect fluorite

phase, suggesting that even high substrate temperatures (1100°C) cannot assist pyrochlore structure formation within the time scale of the deposition process [77]. After heat treatments or thermal cycling of the as-deposited coatings, defect fluorite was found to be ordering into pyrochlore structure. However, although no detrimental effect of this disorder-order transformation on the lifetime has been described, the degree of order in the as-deposited $Ln_2Zr_2O_7$ coatings, kinetics of disorder-order transformation and its possible effects on sintering rate of the coatings have not been reported.

3.4.4. Coefficients of thermal expansion

The CTEs of the dense pyrochlores ($Ln_2Zr_2O_7$, Ln: La, Nd, Sm, Eu, Gd) were reported between 9.1-12.2 x 10^{-6} K^{-1} at 1000 °C (**Table 2**). Although there are significant differences between the results of different studies (see $Gd_2Zr_2O_7$) likely due to different measurement setups, it is clear that CTEs of the pyrochlores are close to that of the standard YSZ 11 x 10^{-6} K^{-1}.

In one of the early studies, two groups of zirconate pyrochlores; (i) $Ln_2Zr_2O_7$, Ln: La, Nd, Eu, Gd with systematically decreasing ion radius and (ii) $La_2Zr_2O_7$ in which La is substituted with one of Nd, Eu and Gd ($La_{1.4}(Nd)_{0.6}Zr_2O_7$, $La_{1.4}(Eu)_{0.6}Zr_2O_7$, $La_{1.4}(Gd)_{0.6}Zr_2O_7$) were investigated [69]. For the first group, no simple dependence of CTE on the Ln cation size was found, except that $La_2Zr_2O_7$ which has the largest Ln cation in the group has the lowest CTE over the studied temperature range (RT-1400 °C). In the second group, CTE of partially substituted compounds was reported to be slightly different than the $La_2Zr_2O_7$ revealing that substitution of 30% La with other trivalent cations does not produce a sufficient distortion in the lattice leading to a significant change in CTEs. Another A-site doping investigation was made on $Gd_2Zr_2O_7$ by Guo et al. [71]. Yb was selected as a dopant element, which has the smallest ionic radii among rare-earth elements and hence reduces the value of rA/rB ratio in $A_2B_2O_7$, resulting in the stabilization of defect fluorite structure instead of the pyrochlore. The CTEs of the Yb_2O_3 doped $Gd_2Zr_2O_7$ ($(Gd_{1-x}Yb_x)_2Zr_2O_7$ (x = 0, 0.1, 0.3, 0.5, 0.7)) were found to be in the range of 11.8x10^{-6} K^{-1} to 13x10^{-6} K^{-1} at 1200°C, which are comparable or even larger than that of the YSZ. Wan et al. investigated a B-site doping of $Gd_2Zr_2O_7$ and chose smaller Ti4+ to partially substitute Zr4+ [78] based on the study of Hess et al. [79], which suggest that the structural integrity of pyrochlore structure is mainly provided by the B-O

bond pair. Therefore weakening of Zr-O bonding may lead a structural relaxation and hence higher CTEs. The CTE of the $Gd_2Zr_2O_7$ was measured to be $11.5x10^{-6}$ K^{-1} at 1000°C in this study which was increased to maximum $11.8x10^{-6}$ K^{-1} by Ti doping ($Gd_2(Zr_{1-x}Ti_x)_2O_7$, x=0.2). A molecular dynamic simulation comparing the effect of A-site and B-site doping on the CTE of $Sm_2Zr_2O_7$ has been performed and the results also showed a higher CTE for the latter ($Sm_2(Ce_{0.3}Zr_{0.7})O_7$) than the former ($(Gd_{0.4}Sm_{0.5}Yb_{0.1})_2Zr_2O_7$) [80]. Therefore in the light of these findings, it can be speculated that the B-site doping in pyrochlore structure can be favorable for a higher CTE, but defect fluorite structure may yield higher CTEs than the pyrochlore structure.

3.4.5.CMAS and Hot Corrosion Behavior

Superior CMAS resistance of $Ln_2Zr_2O_7$ with respect to the YSZ was presented in the last decade, which was a notable finding for the implementation of pyrochlores in TBCs [81,82]. Initially, it was reported for an EB-PVD $Gd_2Zr_2O_7$ TBC that $Gd_2Zr_2O_7$ reacts with the CMAS melt resulting in the crystallization of a highly stable apatite phase incorporating Ca, Gd, and Si at temperatures well above the melting point of the original deposit. This crystalline phase seals off the top of the coating and prevents further CMAS penetration as the reaction and crystallization kinetics are competitive with that for the penetration [83]. Later on, formation of a sealing layer made of $Ca_2Gd_8(SiO_4)_6O_2$ apatite phase was documented for an APS $Gd_2Zr_2O_7$ coating, as well (**Figure 8**). The CMAS penetration depth in the APS $Gd_2Zr_2O_7$ coating was noted as ~20 µm after 24 h interaction at 1200 °C, while it was ~200 µm for the APS YSZ coating under same test conditions. Moreover, infiltration resistance of APS $Gd_2Zr_2O_7$ against different type of molten silicate deposits (e.g.volcanic ash, coal fly ash) was reported in the same study.

Drexler et al. [84] also compared the CMAS resistance of different rare-earth (Yb, Gd, Y) zirconate compositions and a summary of their findings is given in **Table 3**. Based on the results, more than a 10-fold difference in the CMAS penetration depths of YSZ and $Y_2Zr_2O_7$ compositions clearly demonstrated that apatite phase formation and hence the CMAS mitigation resistance is controlled by Y^{3+} concentration in these compositions. Furthermore, different CMAS mitigation performances of the zirconia compositions containing a high concentration of Y_2O_3, Yb_2O_3, and Gd_2O_3 were observed and argued by different sizes of

RE^{3+} as well as the formation of stoichiometrically different apatite phases with CMAS interaction. Authors´ hypothesis was that, as more RE^{+3} cation incorporation is required to form the Gd-type apatite than the Y(or Yb)-type apatite ??? wording the CMAS melt needs to penetrate deeper to accumulate sufficient amount of RE^{+3} in the case of $Gd_2Zr_2O_7$. On the other hand, although they form similar type of apatite phases, shorter penetration depth in $Y_2Zr_2O_7$ than $Yb_2Zr_2O_7$ was attributed to the larger size of Y^{3+} which results in a higher crystallization tendency of Y-apatite.

More recently, Poerschke and Levi systematically investigated the relations between rare-earth oxide (RE: Yb, Gd, La) containing zirconia or hafnia-based compositions and their primary and secondary CMAS interaction products, such as the apatite, fluorite, and garnet [85]. Their results revealed that from the two most relevant reaction products to mitigate CMAS penetration, the apatite and fluorite, the composition of former is relatively insensitive to the composition of the coating material in contrast to what Drexler et al. suggested. They found a strong correlation between the RE cation and the composition of fluorite phase instead. Furthermore, their result suggested that the effectiveness of crystallization reactions increases with larger RE cation sizes (Yb<Gd<La) both in zirconia and hafnia-based systems. Supporting this finding, Schulz and Braue studied the CMAS infiltration response of $La_2Zr_2O_7$ and $Gd_2Zr_2O_7$ coatings deposited with EB-PVD found that the former reacts faster with the CMAS melt than the later [86]. Additionally, their results revealed that the homogeneity of the columnar structure has a profound effect on the reaction kinetics and products as it alters the reaction interfaces and amount of CMAS supply to these reaction zones. Today it is better known that in addition to CMAS composition, viscosity, surface tension of the melts and test temperatures, TBC microstructure, particularly the microstructure of columnar structures e.g. shape of the inter-columnar gaps control the CMAS penetration depth of the same TBC material.

Hot corrosion behavior of pyrochlores has not been investigated as intensive as their CMAS resistance. Marple et al. studied the hot corrosion of $La_2Zr_2O_7$ and YSZ coatings which were exposed to vanadium- and sulfur-containing compounds at temperatures up to 1000 °C [87]. As mentioned earlier, the YSZ coatings are quite vulnerable to vanadium attacks, but they are relatively stable in the presence of sulfur-containing compounds. However, it was revealed with this study that, in contrast to the YSZ, the reaction

of $La_2Zr_2O_7$ with V_2O_5 does not severely damage the coating, while the reactions with sulfur-containing compounds lead to the rapid degradation of the coating under the same test conditions. In another study, superior hot corrosion resistance of $Gd_2Zr_2O_7$ coating than that of the YSZ under $Na_2SO_4 + V_2O_5$ attack at 1050 °C was reported [88]. Different response of pyrochlores against these chemical attacks is evident with these studies compared to YSZ, however defense mechanisms have not been well-understood to this day.

3.4.6. Implementation Issues and Performance

In addition to their advantageous properties, some difficulties have been reported for the application of pyrochlores in TBCs. These issues and their effects on the performance of TBCs will be summarized below.

(i) Thermochemical compatibility with the alumina TGO

Levi [89] demonstrated that when Y_2O_3, Gd_2O_3 and La_2O_3 are added to zirconia above their critical concentrations (Y_2O_3 ~20mol%, Gd_2O_3 ~34mol%, La_2O_3 ~5mol%), formation of garnet, perovskite and β alumina phases, respectively, is induced as a result of an interaction with alumina at 1200°C. Bearing in mind that the $Ln_2Zr_2O_7$ phases are stabilized with ~ 33.3 mol% Ln_2O_3 additions to zirconia, the implication was that all mentioned compositions are prone to degrade by diffusional interaction with Al_2O_3. Later on Leckie et al. experimentally studied the interphase formation between the pre-oxidized sapphire substrates and EB-PVD $Gd_2Zr_2O_7$ coatings [90]. They found that $Gd_2Zr_2O_7$ tends to react with alumina to form a porous $GdAlO_3$ perovskite interphase. A similar phenomenon was also observed between $Sm_2Zr_2O_7$ coatings and alumina in a later study [91]. Therefore, starting with the early patents filed for the pyrochlore implementation in TBC systems, a YSZ inter-diffusion barrier layer was suggested to allow a better performance [92,93]. This also addresses the limited toughness of the pyrochlore materials.

(ii) Fracture toughness

Fracture toughness is a crucial intrinsic factor leading to the 7-8 wt.% yttria-stabilized zirconia with its non-transformable tetragonal (t') phase remains the material of choice for decades. In the 80s, reorientation of ferroelastic domains under applied stress was proposed as a toughening mechanism in tetragonal zirconia explaining particularly the high toughness also at elevated temperatures [94]. Today it is known by

numerous studies that cubic zirconia lacks the benefit of this toughening mechanism and hence exhibit high brittleness. Supporting that, the fracture toughness of tetragonal YSZ was measured to be four times higher than that of cubic $Gd_2Zr_2O_7$ and furthermore, it was suggested that addition of smaller cations (Ti^{4+}) can lead to increased toughness in Gd-doped zirconias, although mechanisms remain elusive [95]. More recently, Dwivedi et al. studied the fracture toughness of YSZ and $Gd_2Zr_2O_7$ free-standing APS coatings in the as-sprayed state and thermally aged conditions [96]. They reported a two times higher fracture toughness of YSZ coating than the $Gd_2Zr_2O_7$ in the as-sprayed state, while the difference further increased after heat treatments. Lower toughness increase of $Gd_2Zr_2O_7$ after thermal treatment was attributed to higher sintering resistance of the material which results in a fewer reduction of the overall porosity as well as less-improved interlamellar bonding.

(iii) Processability and Performance

Vaßen et al. compared the thermal cycling lifetime of the APS $Ln_2Zr_2O_7$ (Ln: La, Gd), APS YSZ, and double layer APS YSZ/ $Ln_2Zr_2O_7$ (Ln: La, Gd) TBC systems under a temperature gradient (1300-1400°C surface and 1070-1090°C bond coat temperatures) [56]. At this high surface temperatures, the lifetime of the double layers was found to be superior to single layer YSZ and $Ln_2Zr_2O_7$ (Ln: La, Gd) systems, revealing that a surface temperature increase of at least 100K compared to standard YSZ (1200°C) possible with the use of $Ln_2Zr_2O_7$, if $Ln_2Zr_2O_7$ are combined with the YSZ interlayer. Later on, the potential of double layer approach was established by several studies using different $Ln_2Zr_2O_7$ compositions or different processing techniques (EB-PVD, SPS) [59,75,91,97]. As an example, **Figure 9** shows the photo and microstructure of an APS $Gd_2Zr_2O_7$/YSZ double layer TBC after thermal cycling, which exhibits a typical TGO growth driven failure after 2055 cycles. At the very similar thermal cycling conditions, lifetime of the standard YSZ is in the range of 1000 cycles which clearly reveals the achieved improvement with this double-layer system.

For more than a decade it has been also known that difference in the vapor pressures of Ln_2O_3 and zirconia complicates the processing of $Ln_2Zr_2O_7$ both with APS and EB-PVD processes. Because the Ln_2O_3 with

higher vapor pressure than zirconia are prone to evaporate at high process temperatures resulting in as-deposited coatings containing metastable zirconia, which transform and then undergo specific volume changes during thermal cycling. There is a paucity of information on the thermodynamic properties of these solid solutions in the literature, however, based on the report of Jacobson it can be generalized that the differences between the vapor pressures of zirconia and Ln_2O_3 increase with decreasing atomic mass of the lanthanide elements [98]. Obviously, the intermolecular bonds get stronger when the atomic mass increases so that it is more difficult to break those bonds to escape as a gaseous phase. Given that the La has smallest atomic mass in the lanthanide series, $La_2Zr_2O_7$ can be expected to be the most problematic pyrochlore composition to deposit, which was stated in a number of APS and EB-PVD studies [57,74,99,100]. In the meantime, only minor compositional changes have been reported for $Sm_2Zr_2O_7$ and $Gd_2Zr_2O_7$ coatings [77,101].

Cao et al. addressed that thermal cycling performance of $La_2Zr_2O_7$ coatings is affected by the fast La_2O_3 loss during the plasma spraying process and this can be prevented to some extent by increasing the amount of La_2O_3 in the feedstock [99]. However, due to the fact that the evaporation rate of the sprayed powder is also influenced by the particle size e.g. vaporization from a small particle will occur sooner than a larger particle, it is not possible to entirely control the homogeneity of the coating composition by this way. Hence, a more sophisticated material related solution is needed in this regard. Mauer et al. reported that burner rig lifetime of a La_2O_3 depleted $La_2Zr_2O_7$ coating can be as short as 14 cycles at 1400°C surface temperature and demonstrated that particle diagnostics can be a useful tool for tuning the particle temperatures during plasma spraying to have the least evaporation [74]. Likewise, Xu et al. showed that the thermal cycling lifetime of EB-PVD $La_2Zr_2O_7$ coatings is affected by non-stoichiometry in the coatings, which can be improved by properly controlling the electron beam current or by changing the ingot composition [102].

4. Summary

In this study, research activities on the developments of TBC ceramic top coats are reviewed. Established and developing thermal spray methods, properties of the state-of-the-art YSZ, as well as emerging ceramic materials, were discussed. The recent TBC literature clearly reveals the potential of lanthanide-zirconate-pyrochlores for further increasing the TBC service temperatures as well as for CMAS protection, while the newer processing technologies are combining high strain tolerance in the top coatings with good cost-efficiency. Nevertheless, use of a double-layer TBC structures including a YSZ layer seems to be a prerequisite for taking advantage of the new materials. Furthermore, deposition of the new materials is proven to be more troublesome than the standard YSZ, meaning much more efforts required to achieve reliable and reproducible processing.

References

1. Forecast International Predicts a World Market for 5,480 Industrial Power Generating Gas Turbine Engines Worth $105 Billion over the Next 10 Years, (https://www.forecastinternational.com/press/release.cfm?article=13562) (Accessed 15.02.2017)
2. Forecast International: 15-Year World Aviation Gas Turbine Market Worth a Staggering $1.2 Trillion, (https://www.forecastinternational.com/press/release.cfm?article=13551) (Accessed 15.02.2017)
3. S. Stecura, Two–Layer Thermal Barrier Coating for High Temperature Components, *Am. Ceram. Soc. Bull.*, **56**(12), 1082-1085 (1978)
4. D.P.H. Hasselman, L.F. Johnson, L.D. Bentsen, S. Rahmatullah, L.L. Hong, M.V. Swain, Thermal Diffusivity and Conductivity of Dense Polycrystalline ZrO$_2$ Ceramics: a Survey, *Am. Ceram. Soc. Bull.*, **66**, 799-806 (1987)
5. L. Pawlowski, D. Lombard, P. Fauchais, Structure-Thermal Properties-Relationship in Plasma Sprayed Zirconia Coatings, *J. Vac. Sci. Technol., A*, **3**(6), 2494-2500 (1985)
6. X.Q. Cao, R. Vassen, D. Stoever, Ceramic materials for thermal barrier coatings, *J. Eur. Ceram. Soc.*, **24**(1), 1-10 (2004)
7. A.G. Evans, D.R. Clarke, C.G. Levi, The influence of oxides on the performance of advanced gas turbines, *J. Eur. Ceram. Soc.*, **28**(7), 1405-1419 (2008)
8. N.P. Padture, M. Gell, E.H. Jordan, Thermal Barrier Coatings for Gas-Turbine Engine Applications, *Science*, **296**(5566), 280-284 (2002)
9. L. Pawlowski, The Science and Engineering of Thermal Spray Coatings, Wiley, 2008
10. S. Kuroda, T.W. Clyne, The quenching stress in thermally sprayed coatings, *Thin Solid Films*, **200**(1), 49-66 (1991)
11. M. Ahrens, R. Vaßen, D. Stöver, S. Lampenscherf, Sintering and creep processes in plasma-sprayed thermal barrier coatings, *J. Therm. Spray Technol.*, **13**(3), 432-442 (2004)
12. G. Gualco, S. Corcoruto, A. Campora, R. Taylor, D. Schwingel, S. Oswald, Highly Porous Thick Thermal Barrier Coatings Produced by Air Plasma Spraying of a Plastic-Ceramic Mixed Powder, Thermal Spray: a United Forum for Scientific and Technological Advances, 1997, pp 305-313

13. W. Gao, Developments in High Temperature Corrosion and Protection of Materials, Elsevier Science, 2008
14. G.P. Cherepanov, R. De Witt, W. Cooley, Mechanics of brittle fracture, McGraw-Hill International Book Co., 1979
15. T.A. Taylor, Thermal properties and microstructure of two thermal barrier coatings, *Surf. Coat. Technol.*, **54**, 53-57 (1992)
16. T.A. Taylor, D.L. Appleby, A.E. Weatherill, J. Griffiths, Plasma-Sprayed Yttria-Stabilized Zirconia Coatings: Structure-Property Relationships, *Surf. Coat. Tech.*, **43-44**(0), 470-480 (1990)
17. H.B. Guo, R. Vaßen, D. Stöver, Atmospheric plasma sprayed thick thermal barrier coatings with high segmentation crack density, *Surf. Coat. Technol.*, **186**(3), 353-363 (2004)
18. M. Peters, K. Fritscher, G. Staniek, W.A. Kaysser, U. Schulz, Design and Properties of Thermal Barrier Coatings for advanced turbine engines, *Materialwiss. Werkstofftech.*, **28**(8), 357-362 (1997)
19. P. Fauchais, R. Etchart-Salas, V. Rat, J.F. Coudert, N. Caron, K. Wittmann-Ténèze, Parameters Controlling Liquid Plasma Spraying: Solutions, Sols, or Suspensions, *J. Therm. Spray Technol.*, **17**(1), 31-59 (2008)
20. E.H. Jordan, C. Jiang, J. Roth, M. Gell, Low Thermal Conductivity Yttria-Stabilized Zirconia Thermal Barrier Coatings Using the Solution Precursor Plasma Spray Process, *J. Therm. Spray Technol.*, **23**(5), 849-859 (2014)
21. H. Kassner, R. Siegert, D. Hathiramani, R. Vassen, D. Stoever, Application of Suspension Plasma Spraying (SPS) for Manufacture of Ceramic Coatings, *J. Therm. Spray Technol.*, **17**(1), 115-123 (2008)
22. A. Guignard, G. Mauer, R. Vaßen, D. Stöver, Deposition and Characteristics of Submicrometer-Structured Thermal Barrier Coatings by Suspension Plasma Spraying, *J. Therm. Spray Technol.*, **21**(3), 416-424 (2012)
23. L. Pawlowski, Suspension and Solution Thermal Spray Coatings, *Surf. Coat. Tech.*, **203**(19), 2807-2829 (2009)
24. N. Curry, K. VanEvery, T. Snyder, N. Markocsan, Thermal Conductivity Analysis and Lifetime Testing of Suspension Plasma-Sprayed Thermal Barrier Coatings, *Coatings*, **4**(3), 630 (2014)
25. K. VanEvery, M.J.M. Krane, R.W. Trice, H. Wang, W. Porter, M. Besser, D. Sordelet, J. Ilavsky, J. Almer, Column Formation in Suspension Plasma-Sprayed Coatings and Resultant Thermal Properties, *J. Therm. Spray Technol.*, **20**(4), 817-828 (2011)
26. K.v. Niessen, M. Gindrat, A. Refke, Vapor Phase Deposition Using Plasma Spray-PVD, *J. Therm. Spray Technol.*, **19**(1-2), 502-509 (2010)
27. S. Rezanka, G. Mauer, R. Vaßen, Improved Thermal Cycling Durability of Thermal Barrier Coatings Manufactured by PS-PVD, *J. Therm. Spray Technol.*, **23**(1-2), 182-189 (2014)
28. R. Vaßen, X. Cao, F. Tietz, D. Basu, D. Stöver, Zirconates as New Materials for Thermal Barrier Coatings, *J. Am. Ceram. Soc.*, **83**(8), 2023-2028 (2000)
29. D.R. Clarke, C.G. Levi, Materials Design For The Next Generation Thermal Barrier Coatings, *Annual Review of Materials Research*, **33**(1), 383-417 (2003)
30. J.L.S. R.A. Miller, R.G. Garlick, Phase Stability in Plasma-Sprayed Partially Stabilized Zirconia-Yttria, The American Ceramic Society, Columbus, OH, 1981
31. H.G. Scott, Phase Relationships in the Zirconia-Yttria System, *J.Mater.Sci.*, **10**(9), 1527-1535 (1975)
32. J. Chevalier, L. Gremillard, A.V. Virkar, D.R. Clarke, The Tetragonal-Monoclinic Transformation in Zirconia: Lessons Learned and Future Trends, *J. Am. Ceram. Soc.*, **92**(9), 1901-1920 (2009)
33. T.J. Marrow, S.G. Roberts, A.K. Pearce-Higgins, The Brittle/Ductile Transition In Cubic Stabilised Zirconia, *J. Eur. Ceram. Soc.*, **14**(5), 447-453 (1994)

34. C. Mercer, J.R. Williams, D.R. Clarke, A.G. Evans, On a Ferroelastic Mechanism Governing the Toughness of Metastable Tetragonal-Prime Yttria-Stabilized Zirconia, *Proceedings of the Royal Society of London A: Mathematical, Physical and Engineering Sciences*, **463**(2081), 1393-1408 (2007)
35. D. Zhu, R. Miller, Thermal Conductivity and Elastic Modulus Evolution of Thermal Barrier Coatings Under High Heat Flux Conditions, *J. Therm. Spray Technol.*, **9**(2), 175-180 (2000)
36. O. Fabrichnaya, F. Aldinger, Assessment of thermodynamic parameters in the system ZrO2–Y2O3–Al2O3, *Zeitschrift für Metallkunde*, **95**(1), 27-39 (2004)
37. S.M. Lakiza, L.M. Lopato, Stable and Metastable Phase Relations in the System Alumina–Zirconia–Yttria, *J. Am. Ceram. Soc.*, **80**(4), 893-902 (1997)
38. J.R. Nicholls, M.J. Deakin, D.S. Rickerby, A Comparison Between the Erosion Behaviour of Thermal Spray and Electron Beam Physical Vapour Deposition Thermal Barrier Coatings, *Wear*, **233-235**(0), 352-361 (1999)
39. R.L. Jones, Some Aspects of the Hot Corrosion of Thermal Barrier Coatings, *J. Therm. Spray Technol.*, **6**(1), 77-84 (1997)
40. R.L. Jones, R.F. Reidy, D. Mess, Scandia, Yttria-stabilized Zirconia for Thermal Barrier Coatings, *Surf. Coat. Tech.*, **82**(1-2), 70-76 (1996)
41. F.H. Stott, D.J. de Wet, R. Taylor, Degradation of Thermal-Barrier Coatings at Very High Temperatures, *MRS Bull.*, **19**, 46-49 (1994)
42. C. Mercer, S. Faulhaber, A.G. Evans, R. Darolia, A Delamination Mechanism for Thermal Barrier Coatings Subject to Calcium-Magnesium-Alumino-Silicate (CMAS) Infiltration, *Acta Mater.*, **53**(4), 1029-1039 (2005)
43. S. Krämer, J. Yang, C.G. Levi, C.A. Johnson, Thermochemical Interaction of Thermal Barrier Coatings with Molten CaO–MgO–Al2O3–SiO2 (CMAS) Deposits, *J. Am. Ceram. Soc.*, **89**(10), 3167-3175 (2006)
44. A. Aygun, A.L. Vasiliev, N.P. Padture, X. Ma, Novel thermal barrier coatings that are resistant to high-temperature attack by glassy deposits, *Acta Mater.*, **55**(20), 6734-6745 (2007)
45. W. Li, H. Zhao, X. Zhong, L. Wang, S. Tao, Air Plasma-Sprayed Yttria and Yttria-Stabilized Zirconia Thermal Barrier Coatings Subjected to Calcium-Magnesium-Alumino-Silicate (CMAS), *J. Therm. Spray Technol.*, **23**(6), 975-983 (2014)
46. P. Ramaswamy, S. Seetharamu, K.J. Rao, K.B.R. Varma, Thermal shock characteristics of plasma sprayed mullite coatings, *J. Therm. Spray Technol.*, **7**(4), 497-504 (1998)
47. N.P. Padture, P.G. Klemens, Low Thermal Conductivity in Garnets, *J. Am. Ceram. Soc.*, **80**(4), 1018-1020 (1997)
48. X. Zhou, Z. Xu, X. Fan, S. Zhao, X. Cao, L. He, Y4Al2O9 ceramics as a novel thermal barrier coating material for high-temperature applications, *Mater. Lett.*, **134**, 146-148 (2014)
49. D.A. Hirschfeld, D.M. Liu, J.J. Brown, CMZP-a new high temperature thermal barrier material, The 4th International Symposium on Ceramic Materials and Components for Engines, R. Carlsson, R. Johansson, L. Kahlman Eds., 1992 (London), Elsevier Applied Science, pp 370-372
50. D. Zhu, R.A. Miller, Development of Advanced Low Conductivity Thermal Barrier Coatings, *International Journal of Applied Ceramic Technology*, **1**(1), 86-94 (2004)
51. D. Zhu, J.A. Nesbitt, C.A. Barrett, T.R. McCue, R.A. Miller, Furnace Cyclic Oxidation Behavior of Multicomponent Low Conductivity Thermal Barrier Coatings, *J. Therm. Spray Technol.*, **13**(1), 84-92 (2004)
52. W. Ma, M.O. Jarligo, D.E. Mack, D. Pitzer, J. Malzbender, R. Vaßen, D. Stöver, New Generation Perovskite Thermal Barrier Coating Materials, *J. Therm. Spray Technol.*, **17**(5-6), 831-837 (2008)

53. M.O. Jarligo, G. Mauer, D. Sebold, D.E. Mack, R. Vaßen, D. Stöver, Decomposition of Ba(Mg1/3Ta2/3)O3 perovskite during atmospheric plasma spraying, *Surf. Coat. Technol.*, **206**(8–9), 2515-2520 (2012)
54. M.O. Jarligo, D.E. Mack, R. Vassen, D. Stöver, Application of Plasma-Sprayed Complex Perovskites as Thermal Barrier Coatings, *J. Therm. Spray Technol.*, **18**(2), 187-193 (2009)
55. W. Ma, D. Mack, J. Malzbender, R. Vaßen, D. Stöver, Yb_2O_3 and Gd_2O_3 Doped Strontium Zirconate for Thermal Barrier Coatings, *J. Eur. Ceram. Soc.*, **28**(16), 3071-3081 (2008)
56. R. Vaßen, F. Träger, D. Stöver, New Thermal Barrier Coatings Based on Pyrochlore/YSZ Double-Layer Systems, *Int. J. Appl. Ceram. Tec.*, **1**(4), 351-361 (2004)
57. B. Saruhan, P. Francois, K. Fritscher, U. Schulz, EB-PVD Processing of Pyrochlore-Structured $La_2Zr_2O_7$-Based TBCs, *Surf. Coat. Technol.*, **182**(2-3), 175-183 (2004)
58. X.Q. Cao, R. Vassen, F. Tietz, D. Stoever, New double-ceramic-layer thermal barrier coatings based on zirconia–rare earth composite oxides, *J. Eur. Ceram. Soc.*, **26**(3), 247-251 (2006)
59. Z. Xu, L. He, R. Mu, X. Zhong, Y. Zhang, J. Zhang, X. Cao, Double-Ceramic-Layer Thermal Barrier Coatings Of $La_2Zr_2O_7$/YSZ Deposited by Electron Beam-Physical Vapor Deposition, *J Alloy Compd.*, **473**(1-2), 509-515 (2009)
60. M.K. Cinibulk, Thermal stability of some hexaluminates at 1400°C, *J. Mater. Sci. Lett.*, **14**(9), 651-654 (1995)
61. R. Gadow, M. Lischka, Lanthanum hexaaluminate — novel thermal barrier coatings for gas turbine applications — materials and process development, *Surf. Coat. Technol.*, **151–152**, 392-399 (2002)
62. G.W. Schäfer, R. Gadow, Lanthanum Aluminate Thermal Barrier Coating, *Ceram. Eng. Sci. Proc.*, **20**(4), 291-297 (1999)
63. X.Q. Cao, Y.F. Zhang, J.F. Zhang, X.H. Zhong, Y. Wang, H.M. Ma, Z.H. Xu, L.M. He, F. Lu, Failure of the plasma-sprayed coating of lanthanum hexaluminate, *J. Eur. Ceram. Soc.*, **28**(10), 1979-1986 (2008)
64. X. Xie, H. Guo, S. Gong, H. Xu, Lanthanum–titanium–aluminum oxide: A novel thermal barrier coating material for applications at 1300 °C, *J. Eur. Ceram. Soc.*, **31**(9), 1677-1683 (2011)
65. M.A. Subramanian, G. Aravamudan, G.V. Subba Rao, Oxide Pyrohlores-A Review, *Prog. Solid St. Chem.*, **15**, 55-143 (1983)
66. F.X. Zhang, M. Lang, R.C. Ewing, Atomic disorder in Gd2Zr2O7 pyrochlore, *Appl. Phys. Lett.*, **106**(19), 191902 (2015)
67. J. Wu, N.P. Padture, P.G. Klemens, M. Gell, E. Garcia, P. Miranzo, M.I. Osendi, Thermal Conductivity of Ceramics in the ZrO_2-$GdO_{1.5}$ System, *J. Mater. Res.*, **17**(12), 3193-3200 (2002)
68. O. Fabrichnaya, R. Wulf, M.J. Kriegel, G. Savinykh, M. Dopita, J. Seidel, H.C. Heitz, O. Nashed, U. Gross, H.J. Seifert, Thermophysical properties of pyrochlore and fluorite phases in the Ln2Zr2O7–Y2O3 systems (Ln = La, Nd, Sm): 1. Pure pyrochlores and phases in the La2Zr2O7–Y2O3 system, *J. Alloys Compd.*, **586**, 118-128 (2014)
69. H. Lehmann, D. Pitzer, G. Pracht, R. Vassen, D. Stöver, Thermal Conductivity and Thermal Expansion Coefficients of the Lanthanum Rare-Earth-Element Zirconate System, *J. Am. Ceram. Soc.*, **86**(8), 1338-1344 (2003)
70. N.P. Bansal, D. Zhu, Effects of doping on thermal conductivity of pyrochlore oxides for advanced thermal barrier coatings, *Materials Science and Engineering: A*, **459**(1-2), 192-195 (2007)
71. L. Guo, H. Guo, H. Peng, S. Gong, Thermophysical properties of Yb2O3 doped Gd2Zr2O7 and thermal cycling durability of (Gd0.9Yb0.1)2Zr2O7/YSZ thermal barrier coatings, *J. Eur. Ceram. Soc.*, **34**(5), 1255-1263 (2014)
72. P.K. Schelling, S.R. Phillpot, R.W. Grimes, Optimum Pyrochlore Compositions for Low Thermal Conductivity, *Philos. Mag. Lett.*, **84**(2), 127-137 (2004)

73. Z. Qu, C. Wan, W. Pan, Thermophysical properties of rare-earth stannates: Effect of pyrochlore structure, *Acta Mater.*, **60**(6–7), 2939-2949 (2012)
74. G. Mauer, D. Sebold, R. Vaßen, D. Stöver, Improving Atmospheric Plasma Spraying of Zirconate Thermal Barrier Coatings Based on Particle Diagnostics, *J. Therm. Spray Technol.*, **21**(3-4), 363-371 (2012)
75. E. Bakan, D.E. Mack, G. Mauer, R. Vaßen, Gadolinium Zirconate/YSZ Thermal Barrier Coatings: Plasma Spraying, Microstructure, and Thermal Cycling Behavior, *J. Am. Ceram. Soc.*, **97**(12), 4045-4051 (2014)
76. I.V. Mazilin, L.K. Baldaev, D.V. Drobot, E.Y. Marchukov, A.M. Akhmetgareeva, Composition and structure of coatings based on rare-earth zirconates, *Inorg. Mater.*, **52**(9), 939-944 (2016)
77. H. Zhao, C.G. Levi, H.N.G. Wadley, Vapor Deposited Samarium Zirconate Thermal Barrier Coatings, *Surf. Coat. Technol.*, **203**, 3157-3167 (2009)
78. C. Wan, Z. Qu, A. Du, W. Pan, Influence of B site substituent Ti on the structure and thermophysical properties of A2B2O7-type pyrochlore Gd2Zr2O7, *Acta Mater.*, **57**(16), 4782-4789 (2009)
79. N.J. Hess, B.D. Begg, S.D. Conradson, D.E. McCready, P.L. Gassman, W.J. Weber, Spectroscopic Investigations of the Structural Phase Transition in Gd2(Ti1-yZry)2O7 Pyrochlores, *The Journal of Physical Chemistry B*, **106**(18), 4663-4677 (2002)
80. F. Qun-bo, Z. Feng, W. Fu-chi, L. Wang, Molecular dynamics calculation of thermal expansion coefficient of a series of rare-earth zirconates, *Computational Materials Science*, **46**(3), 716-719 (2009)
81. M. Freling, M.J. Maloney, D.A. Litton, K.W. Schlichting, J.G. Smeggil, D.B. Snow, Thermal Barrier Coating Compositions, Processes for Applying Same and Articles Coated With Same, *US Patent 7,455,913*, (2008)
82. D.A. Litton, K.W. Schlichting, M. Freling, J.G. Smeggil, D.B. Snow, M.J. Maloney, Durable Reactive Thermal Barrier Coatings, *US Patent 7,662,489*, (2010)
83. S. Krämer, J. Yang, C.G. Levi, Infiltration-Inhibiting Reaction of Gadolinium Zirconate Thermal Barrier Coatings with CMAS Melts, *J. Am. Ceram. Soc.*, **91**(2), 576-583 (2008)
84. J.M. Drexler, A.L. Ortiz, N.P. Padture, Composition effects of thermal barrier coating ceramics on their interaction with molten Ca–Mg–Al–silicate (CMAS) glass, *Acta Mater.*, **60**(15), 5437-5447 (2012)
85. D.L. Poerschke, C.G. Levi, Effects of cation substitution and temperature on the interaction between thermal barrier oxides and molten CMAS, *J. Eur. Ceram. Soc.*, **35**(2), 681-691 (2015)
86. U. Schulz, W. Braue, Degradation of La2Zr2O7 and other novel EB-PVD thermal barrier coatings by CMAS (CaO–MgO–Al2O3–SiO2) and volcanic ash deposits, *Surf. Coat. Technol.*, **235**, 165-173 (2013)
87. B.R. Marple, T.M. Voyer Joël, D.R. Nagy, e. Va/ss, Hot Corrosion of Lanthanum Zirconate and Partially Stabilized Zirconia Thermal Barrier Coatings, *J. Eng. Gas Turbines Power*, **128**(1), 144-152 (2004)
88. M.H. Habibi, L. Wang, S.M. Guo, Evolution of hot corrosion resistance of YSZ, Gd2Zr2O7, and Gd2Zr2O7+YSZ composite thermal barrier coatings in Na2SO4+V2O5 at 1050°C, *J. Eur. Ceram. Soc.*, **32**(8), 1635-1642 (2012)
89. C.G. Levi, Emerging materials and processes for thermal barrier systems, *Curr. Opin. Solid State Mater. Sci.*, **8**(1), 77-91 (2004)
90. R.M. Leckie, S. Krämer, M. Rühle, C.G. Levi, Thermochemical compatibility between alumina and ZrO2–GdO3/2 thermal barrier coatings, *Acta Mater.*, **53**(11), 3281-3292 (2005)
91. H. Zhao, M.R. Begley, A. Heuer, R. Sharghi-Moshtaghin, H.N.G. Wadley, Reaction, Transformation and Delamination of Samarium Zirconate Thermal Barrier Coatings, *Surf. Coat. Technol.*, **205**(19), 4355-4365 (2011)

92. M.J. Maloney, Thermal Barrier Coating Systems and Materials, *US Patent 6,177,200*, (2001)
93. R. Subramanian, Thermal Barrier Coating Having High Phase Stability, *US Patent 6,387,539*, (2002)
94. A.V. Virkar, R.L.K. Matsumoto, Ferroelastic Domain Switching as a Toughening Mechanism in Tetragonal Zirconia, *J. Am. Ceram. Soc.*, **69**(10), C-224-C-226 (1986)
95. R.M.R. Leckie, "Fundamental Issues Regarding the Implementation of Gadolinium Zirconate in Thermal Barrier Coatings," University of California Santa Barbara, 2006
96. G. Dwivedi, V. Viswanathan, S. Sampath, A. Shyam, E. Lara-Curzio, Fracture Toughness of Plasma-Sprayed Thermal Barrier Ceramics: Influence of Processing, Microstructure, and Thermal Aging, *J. Am. Ceram. Soc.*, **97**(9), 2736-2744 (2014)
97. S. Mahade, N. Curry, S. Björklund, N. Markocsan, P. Nylén, R. Vaßen, Functional performance of Gd2Zr2O7/YSZ multi-layered thermal barrier coatings deposited by suspension plasma spray, *Surf. Coat. Technol.*, **Corrected proof**, (2017)
98. N.S. Jacobson, Thermodynamic Properties of Some Metal Oxide-Zirconia Systems, NASA-Lewis Research Center, Cleveland, OH, 1989
99. X.Q. Cao, R. Vassen, W. Jungen, S. Schwartz, F. Tietz, D. Stöver, Thermal Stability of Lanthanum Zirconate Plasma-Sprayed Coating, *J. Am. Ceram. Soc.*, **84**(9), 2086-2090 (2001)
100. Z. Xu, X. Zhong, J. Zhang, Y. Zhang, X. Cao, L. He, Effects of deposition conditions on composition and thermal cycling life of lanthanum zirconate coatings, *Surf. Coat. Technol.*, **202**(19), 4714-4720 (2008)
101. E. Bakan, D.E. Mack, G. Mauer, R. Mücke, R. Vaßen, Porosity-Property Relationships of Plasma-Sprayed $Gd_2Zr_2O_7$/YSZ Thermal Barrier Coatings, *J. Am. Ceram. Soc., Article in Press*, (2015)
102. Z. Xu, X. Zhong, J. Zhang, Y. Zhang, X. Cao, L. He, Effects Of Deposition Conditions on Composition and Thermal Cycling Life of Lanthanum Zirconate Coatings, *Surf. Coat. Technol.*, **202**(19), 4714-4720 (2008)
103. E. Bakan, "Yttria-stabilized zirconia / gadolinium zirconate double-layer plasma-sprayed thermal barrier coating systems (TBCs)," PhD Thesis, Ruhr-Universität Bochum, 2015
104. K.E. Sickafus, L. Minervini, R.W. Grimes, J.A. Valdez, M. Ishimaru, F. Li, K.J. McClellan, T. Hartmann, Radiation Tolerance of Complex Oxides, *Science*, **289**(5480), 748-751 (2000)
105. J.M. Drexler, C.-H. Chen, A.D. Gledhill, K. Shinoda, S. Sampath, N.P. Padture, Plasma sprayed gadolinium zirconate thermal barrier coatings that are resistant to damage by molten Ca–Mg–Al–silicate glass, *Surf. Coat. Technol.*, **206**(19–20), 3911-3916 (2012)
106. G. Suresh, G. Seenivasan, M.V. Krishnaiah, P.S. Murti, Investigation of the Thermal Conductivity of Selected Compounds of Gadolinium and Lanthanum, *J. Nucl. Mater.*, **249**(2-3), 259-261 (1997)
107. C. Wang, "Experimental and Computational Phase Studies of the ZrO_2-Based Systems for Thermal Barrier Coatings," Universität Stuttgart, 2006
108. J. Wang, S. Bai, H. Zhang, C. Zhang, The structure, thermal expansion coefficient and sintering behavior of Nd3+-doped La2Zr2O7 for thermal barrier coatings, *J. Alloys Compd.*, **476**(1–2), 89-91 (2009)
109. W. Ma, X. Li, Y. Yin, H. Dong, Y. Bai, J. Liu, D. Nan, J. Wang, The mechanical and thermophysical properties of La2(Zr1−xCex)2O7 ceramics, *J. Alloys Compd.*, **660**, 85-92 (2016)
110. O. Fabrichnaya, R. Wulf, M.J. Kriegel, G. Savinykh, M. Dopita, J. Seidel, H.C. Heitz, O. Nashed, U. Gross, H.J. Seifert, Thermophysical properties of pyrochlore and fluorite phases in the Ln2Zr2O7–Y2O3 systems (Ln = La, Nd, Sm): 2. Comparison of conventionally sintered and SPS samples in the systems Nd2Zr2O7–Y2O3 and Sm2Zr2O7–Y2O3, *J. Alloys Compd.*, **625**, 200-207 (2015)
111. G. Suresh, G. Seenivasan, M.V. Krishnaiah, P.S. Murti, Investigation of the Thermal Conductivity of Selected Compounds of Lanthanum, Samarium and Europium, *J. Alloys Compd.*, **269**(1-2), L9-L12 (1998)

112. Z. Qu, C. Wan, W. Pan, Thermal Expansion and Defect Chemistry of MgO-Doped Sm2Zr2O7, *Chem. Mater.*, **19**(20), 4913-4918 (2007)
113. H.-s. Zhang, K. Sun, Q. Xu, F.-c. Wang, L. Liu, Preparation and Thermal Conductivity of Sm2(Zr0.6Ce0.4)2O7 Ceramic, *J. Mater. Eng. Perform.*, **18**(8), 1140 (2009)
114. O. Fabrichnaya, M.J. Kriegel, D. Pavlyuchkov, J. Seidel, A. Dzuban, G. Savinykh, G. Schreiber, Heat capacity for the Eu2Zr2O7 and phase relations in the ZrO2–Eu2O3 system: Experimental studies and calculations, *Thermochim. Acta*, **558**, 74-82 (2013)
115. X. Wang, L. Guo, H. Zhang, S. Gong, H. Guo, Structural evolution and thermal conductivities of (Gd1−xYbx)2Zr2O7 (x=0, 0.02, 0.04, 0.06, 0.08, 0.1) ceramics for thermal barrier coatings, *Ceram. Int.*, **41**(10, Part A), 12621-12625 (2015)
116. K.W. Schlichting, N.P. Padture, P.G. Klemens, Thermal conductivity of dense and porous yttria-stabilized zirconia, *Journal of Materials Science*, **36**(12), 3003-3010 (2001)
117. H. Hayashi, T. Saitou, N. Maruyama, H. Inaba, K. Kawamura, M. Mori, Thermal expansion coefficient of yttria stabilized zirconia for various yttria contents, *Solid State Ionics*, **176**(5–6), 613-619 (2005)

Figure captions

Figure 1: Schematic of plasma spraying process with powder injection (left), fracture microstructure of a TBC sample deposited with the APS (right).

Figure 2: Qualitative stress development within different TBCs deposited on a nickel base superalloy during heating (1), dwell time at temperature (2), cooling (3) and at room temperature (4).

Figure 3: Cross section of an as-sprayed SPS YSZ free-standing coating with segmentation cracks (left, [22]) and with columnar structure (right, [25]).

Figure 4: Fracture surface of a columnar YSZ microstructure produced by PS-PVD [27].

Figure 5: Introducing the double-layer structure to the TBCs for higher operation temperatures; schematic illustration of a standard YSZ TBC with the max. temperature capability of 1200°C (left), single layer alternative material TBC with a higher temperature capability which suffers from easy crack propagation and inter-diffusion with the TGO (middle), a double-layer TBC with a YSZ interlayer (right) [103].

Figure 6: The numbers of published items since 2002 covering the topics of TBCs and different material groups according to Web of Science™.

Figure 7: Comparison of the cation (A) and anion (B) arrangements in the unit cells of pyrochlore ($A_2B_2O_7$) and fluorite (MO_2) compounds [104].

Figure 8: Cross-sectional SEM micrograph of APS 7YSZ (left) and $Gd_2Zr_2O_7$ (right) TBCs and corresponding Zr, Ca, and Si elemental maps after interaction with CMAS glass (1200 °C, 24 h). The horizontal dashed line denotes top surface of the original TBC. Reproduced from [105].

Figure 9: Photo (left) and cross-section microstructure (right) showing the failure mode of thermally cycled $Gd_2Zr_2O_7$/YSZ TBC system in burner rig setup. Dashed line on the photo indicates the cutting plane for metallographic sample preparation. The test was conducted at 1394°C/1066°C surface/bond coat temperature gradient and sample failed after 2055 cycles.

Tables

Table 1: Composition of alternative top coat material groups.

Material group	**Composition / Example**
Defect cluster zirconia	ZrO_2-Y_2O_3- Gd_2O_3-Yb_2O_3
Perovskites	➢ Zirconates $AZrO_3$ (A=Sr, Ba, Ca)/ $SrZrO_3$ ➢ Complex forms ABO_3 (A= Ba, La, B=(paired Mg,Ta, Al, La)/ $Ba(Mg_{1/3}Ta_{2/3})O_3$
Hexaaluminates	(La, Nd)$MAl_{11}O_{19}$ (M =Mg, Mn to Zn, Cr or Sm)/ $LaMgAl_{11}O_{19}$
Pyrochlores	➢ $A_2B_2O_7$ A and B are 3+ or 2+ and 4+ or 5+ cations/ $La_2Zr_2O_7$

Table 2: Properties of zirconate pyrochlores with large lanthanides ((La, Nd, Sm, Eu, Gd)Zr_2O_7) vs. YSZ. L, P, and F denote liquid, pyrochlore and fluorite phases, respectively.

Material	**Thermal conductivity at 1000°C (W/mK)**	**Melting temperature/max. stability temperature of pyrochlore or YSZ (°C)**	**CTE (x10^{-6} K^{-1}) at 1000°C**
$La_2Zr_2O_7$	1.8 [106] 1.6 [28] 1.4 [92] 2.1 [70] 2.2 [68] 1.5 [69]	2283/2283(L↔P) [107]	9.7 [108] 9.2 [109] 9.1 [69]
$Nd_2Zr_2O_7$	1.9 [110] 1.3 [69]	2320/2310(F↔P) [107]	9.6 [69]
$Sm_2Zr_2O_7$	1.5 [111] 1.8 [110]	2497/2026(F↔P) [107]	10.8 [112]

	1.3 [113]		
$Eu_2Zr_2O_7$	1.7 [111]	2475/1855(F↔P) [114]	10.5 [69]
$Gd_2Zr_2O_7$	1.4 [106] 1.5 [115] 1.2 [92] 1.2 [71]	2570/1550(F↔P) [107]	10.5 [69] 11.5 [78] 12.2 [71]
8 mol% YSZ	2.1 [116]	2700/1200 [30]	10.1 [117]

Table 3: CMAS mitigation performance of different rare-earth zirconates and their reaction products after 24h CMAS interaction at 1200 °C reported by [84]. Note the different apatite phase stoichiometries of Y and Yb than Gd.

Composition	**Primary phases**	**Phases observed in the reaction zone after CMAS interaction**	**CMAS penetration depth (µm)**
$Y_2Zr_2O_7$ (37.5 mol% Y_2O_3)	Cubic ZrO_2 solid solution	Y-apatite, $Ca_4Y_6(SiO_4)_6O$	20±3
$Gd_2Zr_2O_7$ (38.0 mol% Gd_2O_3)	Fluorite	Gd-apatite, $Ca_2Gd_8(SiO_4)_6O_2$	60±4
$Yb_2Zr_2O_7$ (38.3 mol% Yb_2O_3)	Cubic ZrO_2 solid solution + $Yb_4Zr_3O_{12}$	Yb-apatite, $Ca_4Yb_6(SiO_4)_6O$	40±3
7YSZ (3.9 mol% Y_2O_3)	Tetragonal ZrO_2 solid solution	No apatite phase	263±12

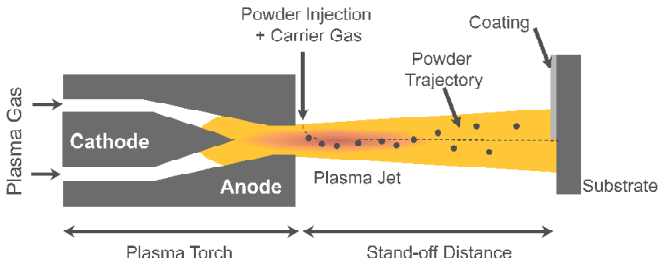

Figure 1: Schematic of plasma spraying process with powder injection (left), fracture microstructure of a TBC sample deposited with the APS (right).

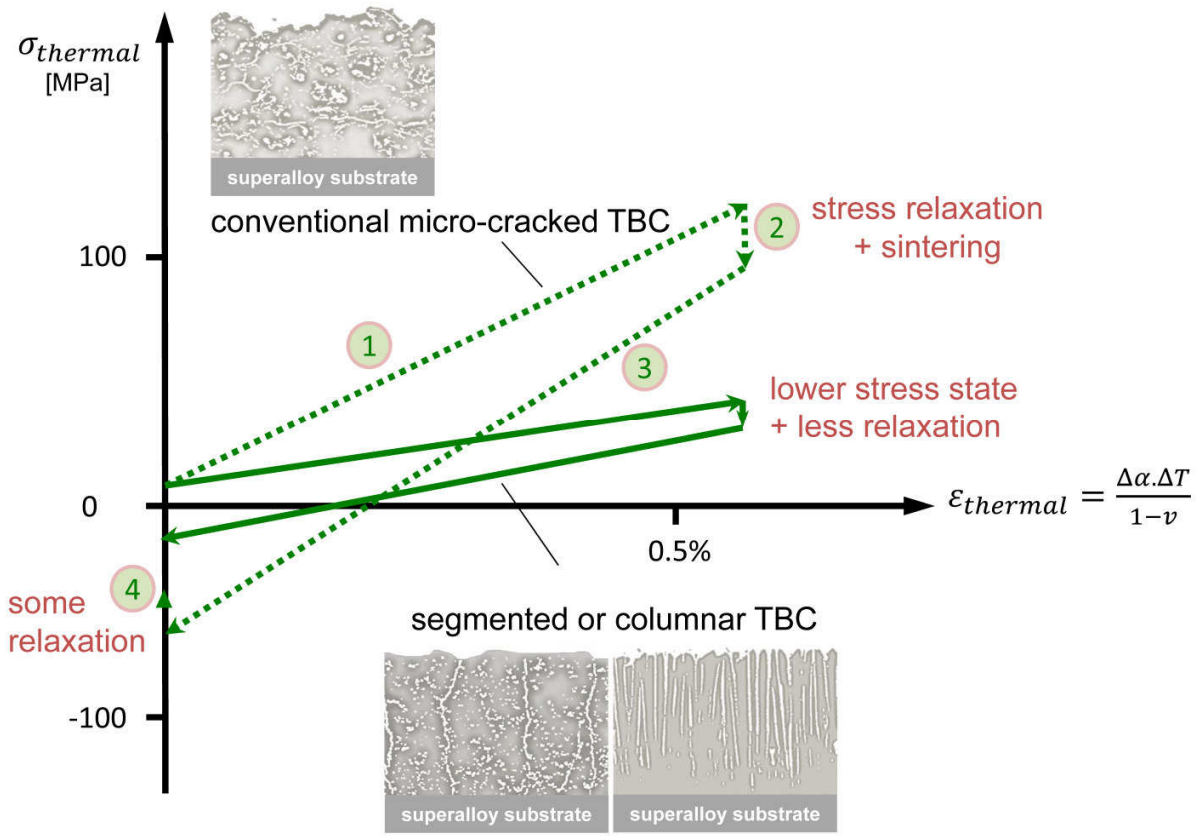

Figure 2: Qualitative stress development within different TBCs deposited on a nickel base superalloy during heating (1), dwell time at temperature (2), cooling (3) and at room temperature (4).

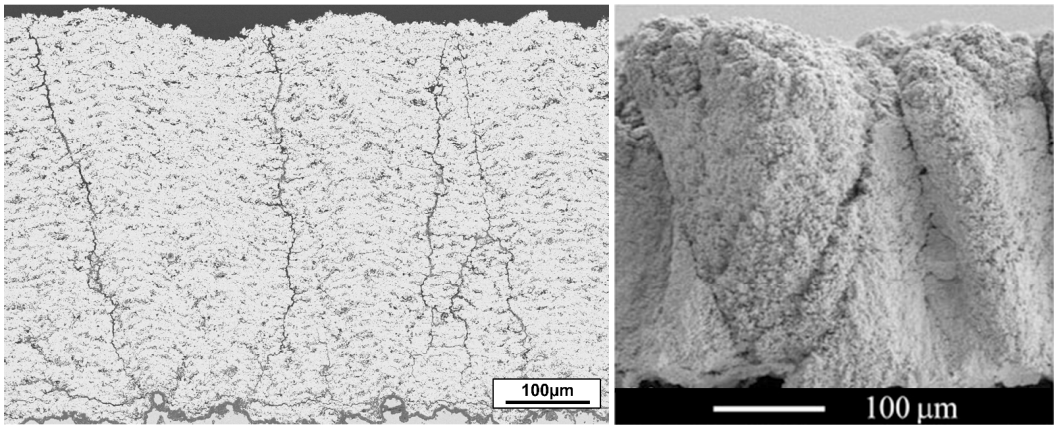

Figure 3: Cross section of an as-sprayed SPS YSZ free-standing coating with segmentation cracks (left, [22]) and with columnar structure (right, [25]).

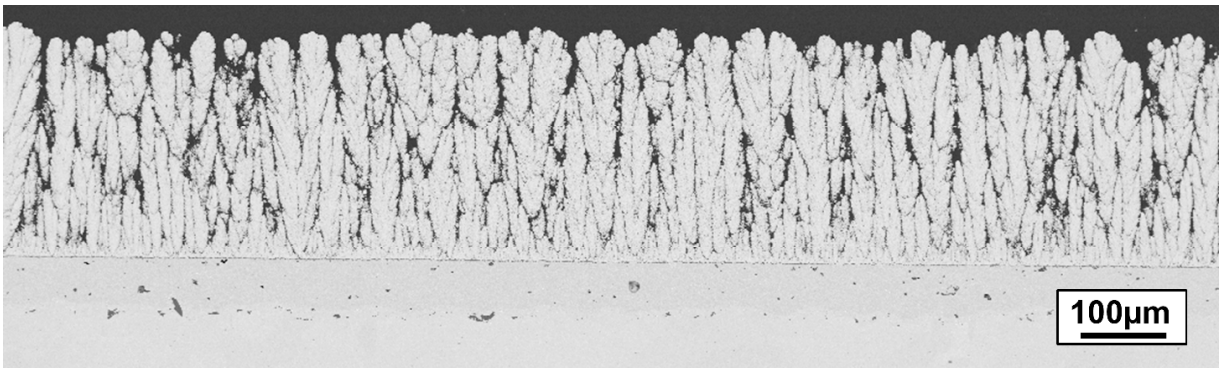

Figure 4: Fracture surface of a columnar YSZ microstructure produced by PS-PVD [27].

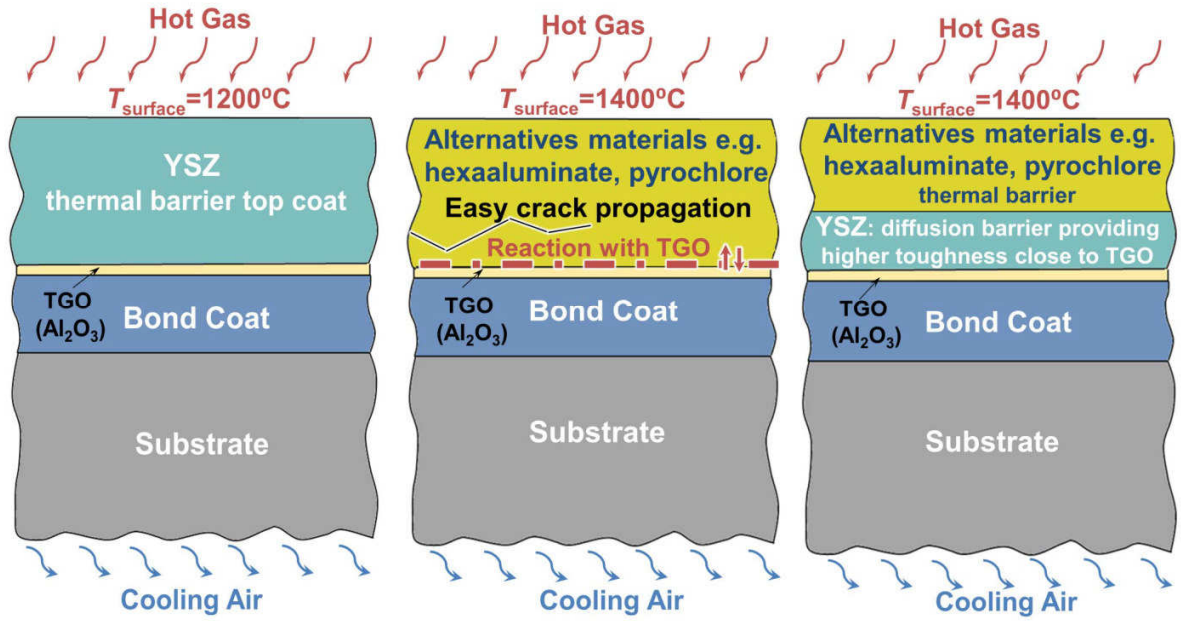

Figure 5: Introducing the double-layer structure to the TBCs for higher operation temperatures; schematic illustration of a standard YSZ TBC with the max. temperature capability of 1200°C (left), single layer alternative material TBC with a higher temperature capability which suffers from easy crack propagation and inter-diffusion with the TGO (middle), a double-layer TBC with a YSZ interlayer (right) [103].

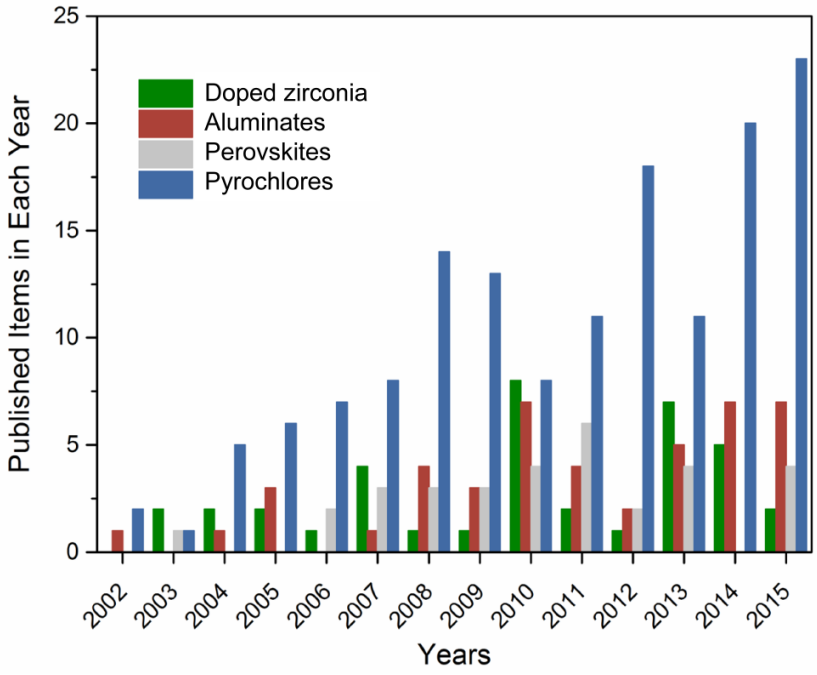

Figure 6: The numbers of published items since 2002 covering the topics of TBCs and different material groups according to Web of Science™.

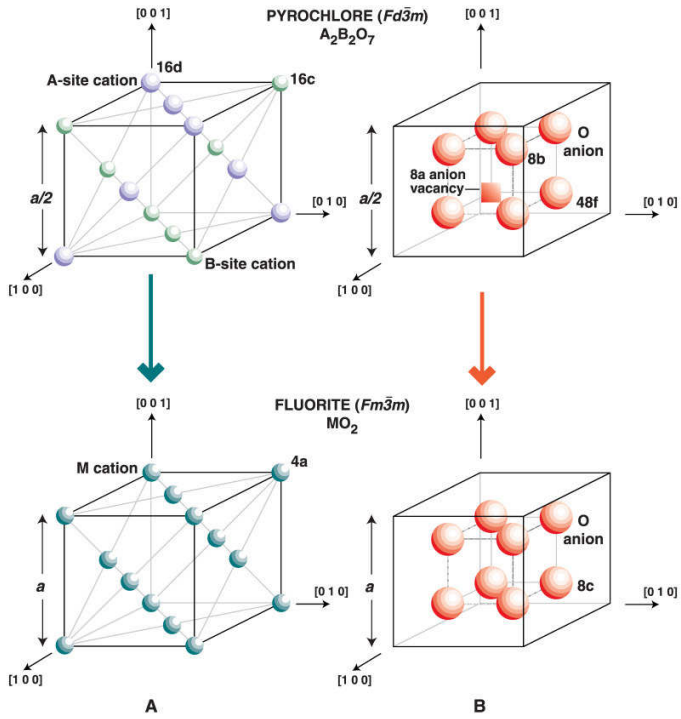

Figure 7: Comparison of the cation (A) and anion (B) arrangements in the unit cells of pyrochlore ($A_2B_2O_7$) and fluorite (MO_2) compounds [104].

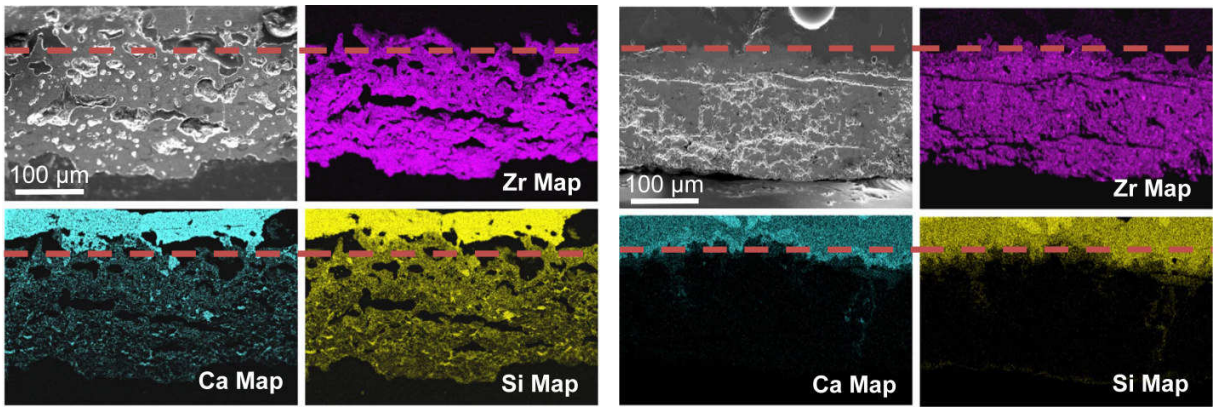

Figure 8: Cross-sectional SEM micrograph of APS 7YSZ (left) and $Gd_2Zr_2O_7$ (right) TBCs and corresponding Zr, Ca, and Si elemental maps after interaction with CMAS glass (1200 °C, 24 h). The horizontal dashed line denotes top surface of the original TBC. Reproduced from [105].

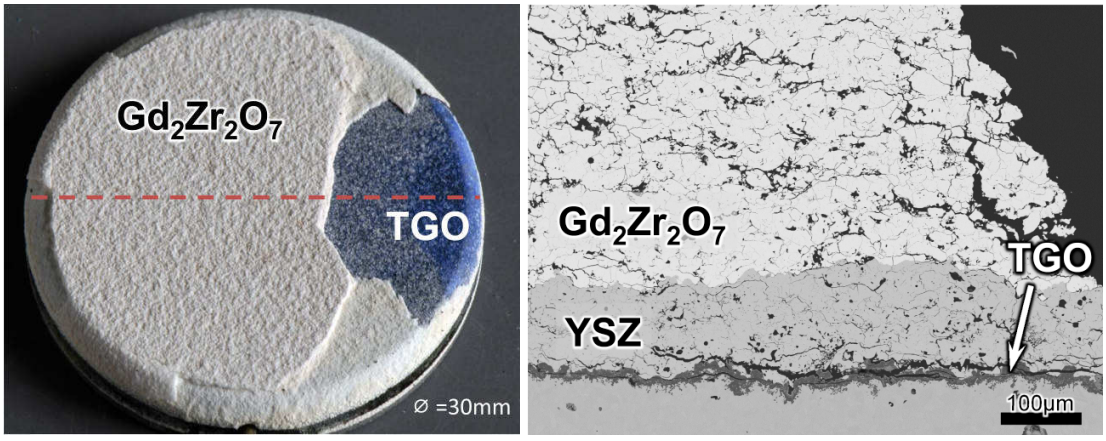

Figure 9: Photo (left) and cross-section microstructure (right) showing the failure mode of thermally cycled $Gd_2Zr_2O_7$/YSZ TBC system in burner rig setup. Dashed line on the photo indicates the cutting plane for metallographic sample preparation. The test was conducted at 1394°C/1066°C surface/bond coat temperature gradient and sample failed after 2055 cycles.